Title

Towards quantitative in vivo dosimetry using x-ray acoustic computed tomography

Journal

Medical Physics, 50(11)

ISSN

0094-2405

Authors

Sun, Leshan

Gonzalez, Gilberto

Pandey, Prabodh Kumar

et al.

Publication Date

2023-11-01

DOI

10.1002/mp.16476

Received: 18 July 2022 | Revised: 5 April 2023 | Accepted: 30 April 2023

DOI: 10.1002/mp.16476

RESEARCH ARTICLE

MEDICAL PHYSICS

Towards quantitative in vivo dosimetry using x-ray acoustic computed tomography

Leshan Sun[1] | **Gilberto Gonzalez**[2] | **Prabodh Kumar Pandey**[3] | **Siqi Wang**[1] | **Kaitlyn Kim**[1] | **Charles Limoli**[4] | **Yong Chen**[2] | **Liangzhong Xiang**[1,3,5]

[1]Department of Biomedical Engineering, University of California, Irvine, California, USA

[2]Department of Radiation Oncology, University of Oklahoma Health Sciences Center, Oklahoma City, Oklahoma, USA

[3]Department of Radiological Sciences, University of California at Irvine, Irvine, California, USA

[4]Department of Radiation Oncology, University of California Irvine, Medical Sciences I, Irvine, California, USA

[5]Beckman Laser Institute, University of California at Irvine, Irvine, California, USA

Correspondence
Liangzhong Xiang, Department of Biomedical Engineering, University of California, Irvine, CA 92617, USA.
Email: liangzhx@hs.uci.edu
Yong Chen,Department of Radiation Oncology,University of Oklahoma Health Sciences Center,Oklahoma City,Oklahoma,USA.
Email: yong-chen@ouhsc.edu

Funding information
National Cancer Institute of the National Institutes of Health, Grant/Award Number: R37CA240806; National Institutes of Health; American Cancer Society, Grant/Award Number: 133697-RSG-19-110-01-CCE; UCI Chao Family Comprehensive Cancer Center, Grant/Award Number: P30CA062203

Abstract

Background: Radiation dosimetry is essential for radiation therapy (RT) to ensure that radiation dose is accurately delivered to the tumor. Despite its wide use in clinical intervention, the delivered radiation dose can only be planned and verified via simulation. This makes precision radiotherapy challenging while in-line verification of the delivered dose is still absent in the clinic. X-ray-induced acoustic computed tomography (XACT) has recently been proposed as an imaging tool for in vivo dosimetry.

Purpose: Most of the XACT studies focus on localizing the radiation beam. However, it has not been studied for its potential for quantitative dosimetry. The aim of this study was to investigate the feasibility of using XACT for quantitative in vivo dose reconstruction during radiotherapy.

Methods: Varian Eclipse system was used to generate simulated uniform and wedged 3D radiation field with a size of 4 cm × 4 cm. In order to use XACT for quantitative dosimetry measurements, we have deconvoluted the effects of both the x-ray pulse shape and the finite frequency response of the ultrasound detector. We developed a model-based image reconstruction algorithm to quantify radiation dose in vivo using XACT imaging, and universal back-projection (UBP) reconstruction is used as comparison. The reconstructed dose was calibrated before comparing it to the percent depth dose (PDD) profile. Structural similarity index matrix (SSIM) and root mean squared error (RMSE) are used for numeric evaluation. Experimental signals were acquired from 4 cm × 4 cm radiation field created by Linear Accelerator (LINAC) at depths of 6, 8, and 10 cm beneath the water surface. The acquired signals were processed before reconstruction to achieve accurate results.

Results: Applying model-based reconstruction algorithm with non-negative constraints successfully reconstructed accurate radiation dose in 3D simulation study. The reconstructed dose matches well with the PDD profile after calibration in experiments. The SSIMs between the model-based reconstructions and initial doses are over 85%, and the RMSEs of model-based reconstructions are eight times lower than the UBP reconstructions. We have also shown that XACT images can be displayed as pseudo-color maps of acoustic intensity, which correspond to different radiation doses in the clinic.

Conclusion: Our results show that the XACT imaging by model-based reconstruction algorithm is considerably more accurate than the dose reconstructed by UBP algorithm. With proper calibration, XACT is potentially applicable to the clinic for quantitative in vivo dosimetry across a wide range of radiation modalities. In addition, XACT's capability of real-time, volumetric dose imaging seems well-suited for the emerging field of ultrahigh dose rate "FLASH" radiotherapy.

KEYWORDS
in vivo dosimetry, model-based reconstruction, quantitative acoustic reconstruction, XACT

1 | INTRODUCTION

In radiation therapy (RT), ionization radiation is used to damage malignant cells.[1] To minimize damage to the peripheral normal tissue bed, treatment planning protocols are developed under image guidance to ensure conformal delivery of the dose. Typically, this involves the superposition of computed tomography (CT) and magnetic resonance (MR) images for treatment planning purposes.[2] However, most treatment plans are generated using pre-acquired CT images, which may not accurately represent the delivered dose as they cannot account for real-time information.[3] During each fraction of treatment, uncertainties in patient setup, tumor shrinkage, organ motion, and variable machine output can affect the actual dose delivered to the tumor and healthy cells.[4,5] The tumor may not be effectively treated if limited dose is received, and healthy organs may be damaged if excessive dose is received. Recently, ultra-high dose rate (FLASH) radiotherapy[6] has become popular for its capability to spare normal tissue toxicities while maintaining iso-effective tumor kill. However, the very high rate of dose delivery makes it even more imperative to precisely monitor the dosimetry during treatment and requires new techniques, such as the one described here for radiation dosimetry.

On-board cone-beam CT (CBCT) was mostly used in the clinic to evaluate pre-treatment patient setup.[7] However, CBCT images are acquired before the treatment starts and cannot account for the intra-fraction tumor motion. Various in vivo radiation dosimetry tools were developed to measure the real-time dose during treatment.[8] By capturing real-time in vivo images of the delivered dose, a patient's treatment plan may be "adapted" over the course of treatment to reflect the changes in the patient and/or tumor anatomy.[9,10] Electronic portal imaging device (EPID) has been considered to be capable of 3D in vivo dosimetry. However, the LINAC gantry needs to be rotated in different angles, making 3D real-time EPID images very challenging. In addition, EPID's detectors are usually made of high atomic number (Z) material, making the response of EPID differ from ion-chamber measurements. Nevertheless, factors like radiation field size and patient-to-EPID distance will affect the mapping of EPID dose to ion-chamber dose.[10–12] In Thermoluminescence detectors (TLDs) and optically simulated luminescence (OSL) were widely used to measure the radiation dose by detecting luminescence light.[13] However, TLDs/OSLs are generally used by placing detectors on the patient's skin near the treatment area and are invasive techniques. Furthermore, they can only measure the dose received at a single point and do not report relevant target dose information. Therefore, the implementation of adaptive radiotherapy is limited by the lack of a real-time monitoring device that can accurately measure the delivered dose in vivo non-invasively.

In 2013, x-ray-induced acoustic tomography (XACT) was first proposed for biomedical purposes.[14] In XACT imaging, pulsed x-rays excite the target, resulting in rapid localized heating (<mK). The abrupt temperature increase leads to thermoelastic expansion that causes differential pressure distribution.[15,16] The local pressure difference causes the emission of a detectable acoustic wave in the ultrasound regime.[17,18] The amplitude of the acoustic signal is proportional to the deposited heat energy, making it a potential tool for radiation dosimetry. Furthermore, the induced x-ray acoustic (XA) wave will propagate in all directions and can be detected at various transducer positions. Various research has been conducted to investigate the feasibility of using XACT for 3D real-time *radiation* dosimetry,[19–22] as its numerous advantageous characteristics make it a promising technique for water tank dosimetry applications. XACT depends on the dose deposited per pulse, meaning energy and dose rate can be considered independent. Also, XACT does not perturb the radiation beam provided the transducers are placed outside the beam path.[19] These features of XACT simplify calibration and eliminate the need for correction factors, which are required by other dosimetry techniques.[23] Unlike conventional diagnostic acoustic imaging techniques that image the structure of tissue,[24] the aim of XACT dosimetry is to image the acoustic sources induced by the x-ray dose deposition within the patient. Thus, quantitative in vivo dosimetry could be possible using XACT imaging if the parameters are properly modeled, and if the transducer and amplification system are well calibrated and characterized. However, the current limitations in XACT imaging make it impossible to quantitatively reconstruct dose.[14,19,21] One of the challenges in XACT imaging is the relatively long pulse duration ($\sim$4 μs), which would affect both the signal generation efficiency and imaging resolution.[25,26] Deconvolution of the detected transducer signals from the LINAC pulse shape could be an effective approach to resolve this problem.[27] Another key challenge of XACT is its sensitivity to detecting small amplitude acoustic waves.[28] Improvements in detection amplification will be necessary to accurately image radiation fields without the need for excessive signal averaging. Additionally, deconvolution of the transducer's frequency response can further improve signal detection accuracy.[27,29,30] More sophisticated signal processing and image

reconstruction techniques are expected to be useful for obtaining accurate XACT image reconstruction. Iterative time-reversal (ITR) algorithm has been proposed to quantitatively reconstruct dose information, but it lacks experimental validation and cannot model the characteristics of different transducers, such as reception angles.[20]

In this study, we mathematically modeled the generation and propagation of XA signals to quantitatively reconstruct 3D dose information.[31] We have deconvoluted the effects of both the x-ray pulse shape and the finite frequency response of the ultrasound detector[27] to improve the accuracy of XACT image reconstruction. Both 3D simulations and experimental measurements have been performed for quantitative dosimetry. Previous in vivo dosimetry tools could only get dose information for skins or relative dose information for tumors.[8] Here, we propose to use XACT to reconstruct 3D quantitative dosimetry, which can potentially be used to monitor the dose received by tumor during treatment. We validated the XACT reconstruction results with both simulation data and experimental data.

2 | MATERIALS AND METHODS

2.1 | Generation and propagation of x-ray induced acoustic wave

In XACT, x-rays will cause temperature rise in its absorbing target, which will lead to the generation of acoustic signals. The generation and propagation of XA signal under the assumptions of thermal confinement and zero acoustic attenuation can be expressed as:

$$\left(\nabla^2 - \frac{1}{c^2}\frac{\partial^2}{\partial t^2}\right) p\left(\vec{r}, t\right) = -\frac{\beta}{C_p}\frac{\partial H\left(\vec{r}, t\right)}{\partial t} \quad (1)$$

where $p(\vec{r}, t)$ denotes the acoustic pressure at location $\vec{r}$ and time t, c is the speed of sound, β is the thermal expansion coefficient, Cp denotes the target's heat capacity at a constant pressure, and $H(\vec{r}, t)$ is the heating function.

The heating function H is related to the deposited dose per unit time,[1] D and can be written as:

$$H = \eta_{th} D\rho \quad (2)$$

where η_{th} is the percentage of dose energy converted into thermal energy and ρ is the density of the absorption target. Thus, Equation (1) can be rewritten as:

$$\left(\nabla^2 - \frac{1}{c^2}\frac{\partial^2}{\partial t^2}\right) p\left(\vec{r}, t\right) = -\frac{\eta_{th}\rho\beta}{C_p}\frac{\partial D\left(\vec{r}, t\right)}{\partial t} \quad (3)$$

The dose deposited by the pulsed radiation will cause an abrupt increase in temperature. The right-hand side of Equation (1) represents the thermal expansion caused by the temperature rise. The thermal expansion then becomes the source of acoustic wave, and its propagation is modeled by the left-hand side of Equation (1).

2.2 | Acoustic forward problem

The forward model deals with the prediction of the acoustic fields dominated by Equation (3). The solution to Equation (3) is given by[32]:

$$p\left(\vec{r}, t\right) = \frac{\Gamma\eta_{th}\rho}{4\pi c}\frac{\partial}{\partial t}\left(\frac{1}{ct}\int_{S\left(\vec{r},t\right)} D\left(\vec{r}', t\right) dS'(t)\right) \quad (4)$$

where $\Gamma(c^2\beta/C_p)$ is the Gruneisen parameter. $S'(t)$ denotes a spherical surface that all points on the surface satisfy $|\vec{r} - \vec{r}'| = ct$. If the problem is 2D, $S'(t)$ will reduce to a curved line that satisfies the same condition.

For a certain absorption material, the density, absorption rate, and Gruneisen parameter are constant values.[20] Therefore, we can let $\Phi = \frac{\Gamma\eta_{th}\rho}{4\pi c}$, which is a constant (unit $\mathrm{kg \cdot s/m^4}$) that only depends on material types, and Equation (4) can be further simplified as:

$$p\left(\vec{r}, t\right) = \Phi\frac{\partial}{\partial t}\left(\int_{S\left(\vec{r},t\right)} D\left(\vec{r}', t\right) d\theta\right) \quad (5)$$

To analytically solve the equation, discretization[31] was performed by approximating surface $S'(t)$ by a set of N points that are equally distributed according to space angles. Equation (5) can then be rewritten as:

$$p\left(\vec{r}, t\right)/\Phi = \frac{I(t + \Delta t) - I(t - \Delta t)}{2\Delta t} \quad (6)$$

where $I(t)$ is the discretized integration of $D(\vec{r}', t)$, and can be expressed as:

$$I(t) = \sum_{l=1}^{N} D\left(\vec{r}_l', t\right) d\theta \quad (7)$$

By combining Equations (6) and (7), the pressure at transducer position $\vec{r}_i$ and time t_j $p(\vec{r}_i, t_j)$ can be

expressed as a linear combination of the absorbed dose at positions $\vec{r}'_l$:

$$p\left(\vec{r},t\right) = \Phi \sum_{l=1}^{N} a_l^{i,j} D\left(\vec{r}'_l,t\right) \tag{8}$$

where $a_l^{i,j}$ are the linear interpolation coefficients that were used to obtain $D(\vec{r}'_l,t)$.

With Equation (8), the acoustic forward problem can be modeled as

$$\mathbf{p} = \Phi\mathbf{M}\mathbf{D} \tag{9}$$

where $\mathbf{p}$ is the pressure signal, $\mathbf{M}$ is the model matrix constituted of $a_l^{i,j}$, and $\mathbf{D}$ is the initial dose distribution map.

2.3 | Image reconstruction

The back-projection (BP) algorithms are commonly employed because of their simplicity and easy implementation.[32,33] However, BP reconstruction comes with many inaccuracies in quantification reconstructions due to the limited transducer reception angle and the loss of low-frequency information.[34–38] Therefore, to reconstruct dose information with higher accuracy, model-based reconstruction was employed in this study, and universal back-projection (UBP) reconstruction was used as a comparison.

The model-based reconstruction is based on the model matrix $\mathbf{M}$ computed in Section 2.2. $\mathbf{M}$ only depends on the geometry of the system setup and the characteristics of the material. Therefore, XACT image reconstruction is performed by minimizing the mean square difference between the theoretical pressure $\mathbf{p}$ and the measured pressure $\mathbf{p}_m$:

$$\mathbf{D_{sol}} = \arg\min_{\mathbf{D}\geq 0} \|\mathbf{p}_m - \mathbf{M}\mathbf{D}\|^2 \tag{10}$$

where $\mathbf{D_{sol}}$ is the reconstructed dose map. As the reconstructed dose cannot be negative. we applied non-negative constraints $\mathbf{D} \geq 0$ to eliminate negative values for the reconstructed dose map.[39] The non-negative constraints were lifted when investigating the shape of the field and applied when doing quantitative reconstruction. The solution of Equation (10) is given as[40]:

$$\mathbf{D_{sol}} = \left(\mathbf{M}^T\mathbf{M} + \lambda^2\,\mathbf{R}^T\mathbf{R}\right)^{-1}\,\mathbf{M}^\mathbf{T}\mathbf{p}_m \tag{11}$$

where $\mathbf{R}$ is the regularization matrix and λ is the parameter for the regularization. In our study, we use an identity matrix for $\mathbf{R}$ as Tikhonov regularization. Since matrix $\mathbf{M}^T\mathbf{M} + \lambda^2\,\mathbf{R}^T\mathbf{R}$ is a large sparse matrix, MATLAB LSQR[41] function was implemented to calculate the approximate inverse matrix of $\mathbf{M}^T\mathbf{M} + \lambda^2\,\mathbf{R}^T\mathbf{R}$.

2.4 | 3D dose simulation

Simulation studies were first performed to test the feasibility of using XACT for quantitative dose reconstruction. To simulate dose distribution, we first generated a 4 cm × 4 cm uniform square radiation field in water using the Varian Eclipse system.[42]

As XA signals propagate in the form of spherical waves, we set up a 3D cylindrical transducer array to receive full-view signal. Figure 1 shows the setup for the 3D cylindrical array simulation. Figure 1a shows the horizontal view of the simulation setup. The radius of the cylinder is 9 cm and the center is set to be the radiation field's center. Ninety transducers are arranged as a circle on one horizontal plane with an interval of roughly 5 mm. Figure 1b shows the vertical view of the simulation setup. There are 40 horizontal planes equally distributed from the water surface to 20 cm depth under the surface with 5 mm intervals to match with the ring array transducer interval. Therefore, the cylindrical transducer array has 3600 transducers in total. No transducer is placed on the top and bottom of the cylinder as it would block the x-ray beam.

To account for an acquisition scenario from a real transducer, we implemented the angular directivity[43] in our forward signal simulation. The reception cone is shown in Figure 1b and its angle was calculated to be 20° based on the Olympus technical note.[44] The simulation signal was generated using the method described in Section 2.2. The accuracy of the generated signal has been validated using the k-Wave toolbox in our previous work.[40]

In addition to uniform dose field simulation, we also generated a 4 cm × 4 cm wedged dose field using the Varian Eclipse system. The wedge was chosen to be 45° to give a clear dose drop in the 4 cm field size. The same simulation settings were used for this wedged field.

The simulated 3D signals were reconstructed using both the UBP reconstruction and model-based reconstruction described in Section 2.3. Both reconstruction results are compared to the initial dose distribution for analysis. For quantitative evaluation, we calculated the structural similarity index matrix (SSIM)[45] and root mean squared error (RMSE)[46] for selected 2D slices from the 3D reconstruction. SSIM is used to evaluate the structural similarity between the reconstructed dose and original dose, while RMSE is used to evaluate the quantitative difference.

SSIM is defined as

$$\mathrm{SSIM} = \frac{\left(2\mu_R\mu_I + c_1\right)\left(2\sigma_{IR} + c_2\right)}{\left(\mu_R^2 + \mu_I^2 + c_1\right)\left(\sigma_R^2 + \sigma_I^2 + c_2\right)} \tag{12}$$

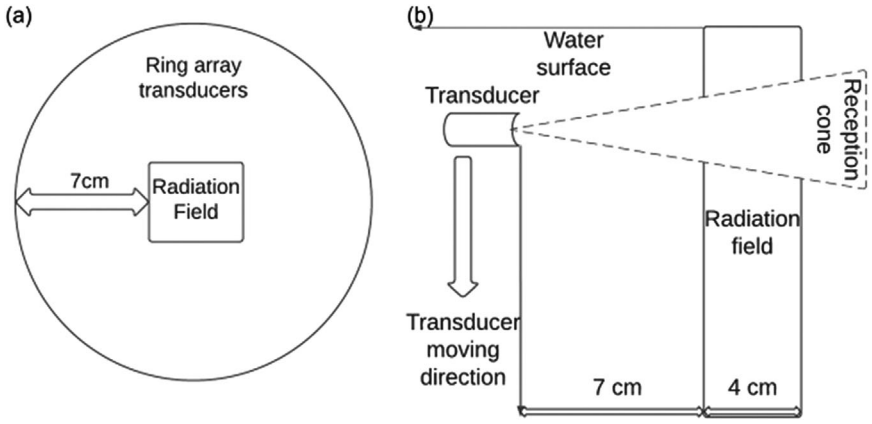

FIGURE 1 Illustration of 3D simulation setup. (a) Horizontal view of the simulation setup. Ninety transducers are distributed equally on the circle with 4° angular interval. The radius of the circle is set to be 9 cm (the distance from transducer to the edge is 7 cm). The radiation field is a 4 cm × 4 cm square. (b) Vertical view of the simulation setup. The transducer is moving from the water surface to 20 cm depth under the water surface with 5 mm interval to form a cylindrical array. The reception cone of the transducer is set to be around 20° according to the Olympus technical notes.

where R and I denote the reconstructed images and initial dose distribution, respectively. μ_R is an average of R, σ_I^2 is a variance of I and σ_{IR} is a covariance of I and R. There are two variables to stabilize the division, such as $c_1 = (k_1 L)^2$ and $c_2 = (k_2 L)^2$. L is a dynamic range of pixel intensities. k_1 and k_2 are constants by default, where $k_1 = 0.01$ and $k_2 = 0.03$. RMSE is defined as

$$\mathrm{RMSE} = \sqrt{\frac{\sum_{n=1}^{N} (r_n - i_n)^2}{N}} \tag{12}$$

where N is the number of pixels in the selected 2D slice, r_n and i_n are the values at pixel number n from reconstructed images and initial dose distribution, respectively. Both SSIM and RMSE are calculated using MATLAB built-in functions.[47,48]

2.5 | 2D real signal simulation

It is impossible to put one transducer at 3600 different positions to acquire 3D signal information as it would take hundreds of hours, and the radiation field would vary in day-to-day experiments. Therefore, we performed a circular array simulation which can be carried out clinically. The 2D simulation only uses 90 transducer signals on one horizontal plane to perform the 2D reconstruction.

In addition, the simulated signal generated from the forward method in Section 2.2 is an ideal signal with infinite transducer bandwidth and infinite pulse duration. However, in clinical experiments, the LINAC x-ray pulse duration is about 4 ¯s and the transducer only has a narrow bandpass range. Both factors will largely affect the shape and amplitude of the XA signal.

To simulate a realistic signal, we first generated a 4 ¯s square x-ray pulse[21] and performed the numerical convolution of the x-ray pulse with the XA signal generated in Section 2.4 using Equation (13):

$$p_{conv}(t) = \sum_{\tau=1}^{t} p(\tau)\, S(t-\tau) \tag{13}$$

where p_{conv} is the convoluted signal, p is the ideal signal from Equation (8), and $S(t)$ is the LINAC x-ray pulse width. All terms are discretized for analytical calculation.

A bandpass filter was then applied to the convoluted signal to simulate the signals that are detected by limited bandwidth transducer. The frequency spectrum of the bandpass filter is a gaussian function with a center frequency of 500 kHz and 100% bandwidth for −6 dB. The frequency spectrum was applied to the convoluted signal in the frequency domain using Equation (14):

$$p_{real}(t) = \mathcal{F}^{-1}(P(f) \times F(f)) \tag{14}$$

where p_{real} is the detected signal with limited bandwidth transducer, $P(f)$ is the Fourier transform of p_{conv}, and $F(f)$ is the gaussian frequency spectrum.

In the final process of the signal, both low-frequency random noise and high-frequency gaussian white noise were added to the signal to simulate the real scenario.

To perform image reconstruction with the simulated real signal, both low-pass and high-pass noise filters were added to eliminate the noise. After applying the filters, the frequency spectrum was divided from the signal's frequency domain and deconvolution of the x-ray pulse width was performed to get the ideal signal. The reconstructed doses are normalized using the PDD profile to evaluate the reconstruction.

2.6 | Experiment workflow

Experimental signals were acquired by irradiating a water tank using a clinical radiotherapy LINAC (Varian Medical Systems, Palo Alto, CA, USA). The radiation beam was set to be a 10 MV flattening filter free (FFF) photon beam produced by a True-Beam LINAC. The dose rate of the LINAC was set to 2400 MU/min and the repetition rate was 120 Hz. Figure 2 shows the experimental setup. The water tank was placed on the LINAC couch at a source-to-surface distance (SSD) of 100 cm.

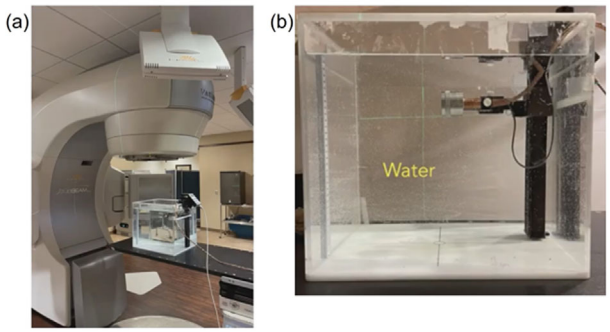

FIGURE 2 Photograph of experimental set-up. (a) Water tank was placed on the LINAC couch. (b) The immersion ultrasound transducer was set to be able to move in z direction inside the water tank. The preamplifier and the data acquisition (DAQ) system are not pictured in this photograph.

The scheme of the experimental setup is similar to the illustration in Figure 1. We used an unfocused immersion Olympus ultrasonic transducer with a central frequency of 0.5 MHz and –6 dB bandwidth of 80%. The element size of the transducer is 1.5 inches in diameter. The transducer was placed 9 cm away from the isocenter in the water and the radiation field was set to be 4 cm × 4 cm. The transducer was placed in the water to avoid the acoustic impedance mismatch caused by the water tank wall. This also suits non-invasive clinic scenarios as acoustic gel will be applied between the ultrasound transducer and the patient's skin to avoid acoustic impedance mismatch. Instead of rotating the transducer in a circle, the LINAC collimator was rotated 360° with 4° angular intervals. By doing this, the background noise caused by the movement of water can be greatly reduced.

The experimental signal was first processed according to the procedures described in Section 2.5. before doing the image reconstruction. Both UBP and model-based reconstruction were performed for comparison.

3 | RESULTS

3.1 | 3D quantitative dose simulation

The first simulation used a 3D transducer array to demonstrate the capability of using XACT for dose imaging. Figure 3a,d shows the horizontal and vertical view of the generated initial dose distribution from Varian Eclipse system. The representative horizontal slice is taken at 6 cm depth. Figure 3b,e shows the reconstructed UBP image while Figure 3c,f shows the model-based reconstruction results. The model-based reconstruction clearly has better image quality than the UBP reconstruction. The model-based reconstructed dose distribution map matches well with the initial dose distribution map, which can also be seen in Table 1. There are slight differences at the top and bottom of the vertical image. This is because transducers at the top and bottom have some parts of their reception cones that lie outside the image range, which causes inaccuracy in the reconstructed images.

Figure 4 shows the model-based reconstruction for wedged field. In Figure 4b,e, there are some artifacts around this non-uniform radiation field that do not exist in the uniform field. This is because the signals received by transducers on the same horizontal plane will have different amplitudes and the limited reception angle of the transducer will result in a limited-view problem in this artifact area. Nevertheless, the reconstructed dose quantity matches well with the initial dose distribution, which can also be seen in the dose profile comparison in Figure 4c,f and Table 1. In addition, the dose profiles do not match well at the top and bottom of the radiation field, which is the same problem as the uniform field reconstruction caused by transducer reception cones lying outside the image range.

3.2 | 2D real signal simulation

In the clinic, it is impossible to have a 3D transducer array that covers the whole radiation field. Therefore, the second simulation attempts to perform the dose reconstruction in 2D using a circular array. In addition, the XA signal is generated from the LINAC x-ray pulse, which has a longer pulse duration than a laser and cannot be seen as a delta pulse. In the 2D simulation, these properties were taken into account, and the simulated real signal was generated to match the experimental signal. The ideal simulated signal is extracted from the 3D simulation in Section 3.1. It is generated with infinite bandwidth and x-ray pulse width. The signal is convoluted with a 4 ¯s x-ray pulse and 0.5 MHz central frequency response. 20 dB low- and high-frequency noises are added to the signal. 20 kHz high-pass filter and 200 kHz low-pass filter was first applied to eliminate the noise. The signal was then divided by the same frequency spectrum used in generating the simulated real signal in the frequency domain. In the end, deconvolution with the 4 ¯s x-ray pulse was performed to get the processed signal for reconstruction.

The ideal, real, and processed signals were then used to reconstruct the XACT images to investigate the effects of using different signals. Figure 5 shows the comparison between the reconstruction results using these signals. Figure 5a is the reconstructed image 6 cm under the water surface using the ideal simulated signal. Despite some artifacts around the image caused by the limited angular directivity of the transducer, the reconstruction shows a clear shape of the radiation field. However, the dose range of the reconstruction is different from the initial pressure demonstrated in Figure 3a because the simulated signal is generated in 3D while

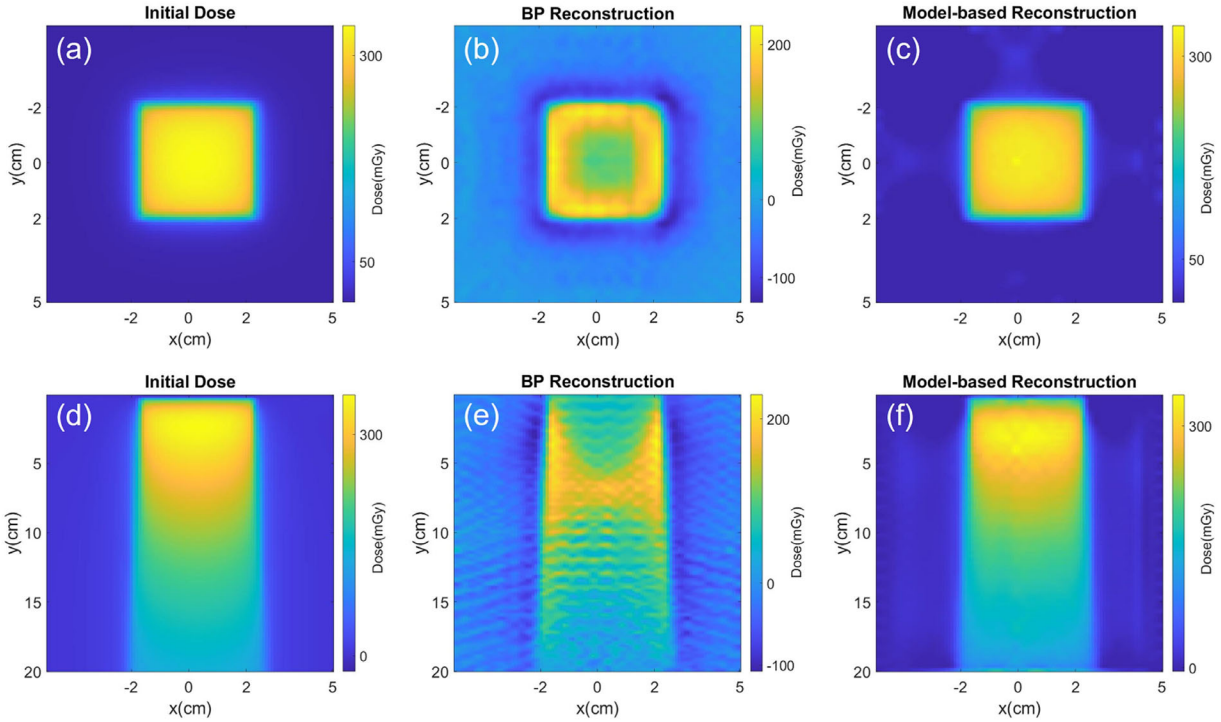

FIGURE 3 Simulated 3D reconstruction. (a) Initial dose for horizontal plane at 6 cm depth. (b) Universal back-projection for horizontal plane at 6 cm depth. (c) Model-based reconstruction for horizontal plane at 6 cm depth. (d) Initial dose for vertical plane at isocenter. (e) Universal back-projection for vertical plane at isocenter. (f) Model-based reconstruction for vertical plane at isocenter.

TABLE 1 2D quantitative evaluation for simulation reconstruction.

	Uniform field		Wedged field	
	Horizontal plane at 6 cm depth	Vertical plane at radiation center	Horizontal at 6 cm depth	Vertical plane at radiation center
Model-based reconstruction				
SSIM	0.863	0.890	0.869	0.893
RMSE	8.22	4.28	10.57	5.47
Universal back projection				
SSIM	0.161	0.077	0.086	0.080
RMSE	66.01	33.63	53.90	30.95

Abbreviations: RMSE, root mean squared error; SSIM, structural similarity index matrix.

the reconstruction is performed in 2D. Figure 5b shows the reconstructed image using the simulated real signal. The edge of the reconstructed radiation is blurry, and the size of the radiation field is about 5 cm, which is larger than the initial radiation field. This is because the convolution of the 4 ¯s x-ray pulse enlarged the radiation field by roughly 6 mm. Figure 5c shows the image reconstructed from the processed signal. The limited-angle artifact was enlarged due to the presence of noise and the edge of the radiation field has a slight distortion. Overall, the shape of the reconstructed radiation field is satisfactory, and the range of the reconstructed dose is similar to Figure 5a. Figure 5d shows the comparison between the reconstructed dose and the LINAC PDD profile. The 2D reconstructions were performed at varying depths of 4, 6, 8, 10, and 15 cm. The reconstructed dose is normalized at a depth of 4 cm. The reconstruction results align well with the PDD profile. The 2D reconstruction results show that, in order to reconstruct accurate radiation field, the detected real signal must be processed before doing the reconstruction.

3.3 | Experiment result

To test XACT's capability of quantitative dosimetry in the clinic, an experimental study using Varian LINAC machine was performed. A ring array XA signal was

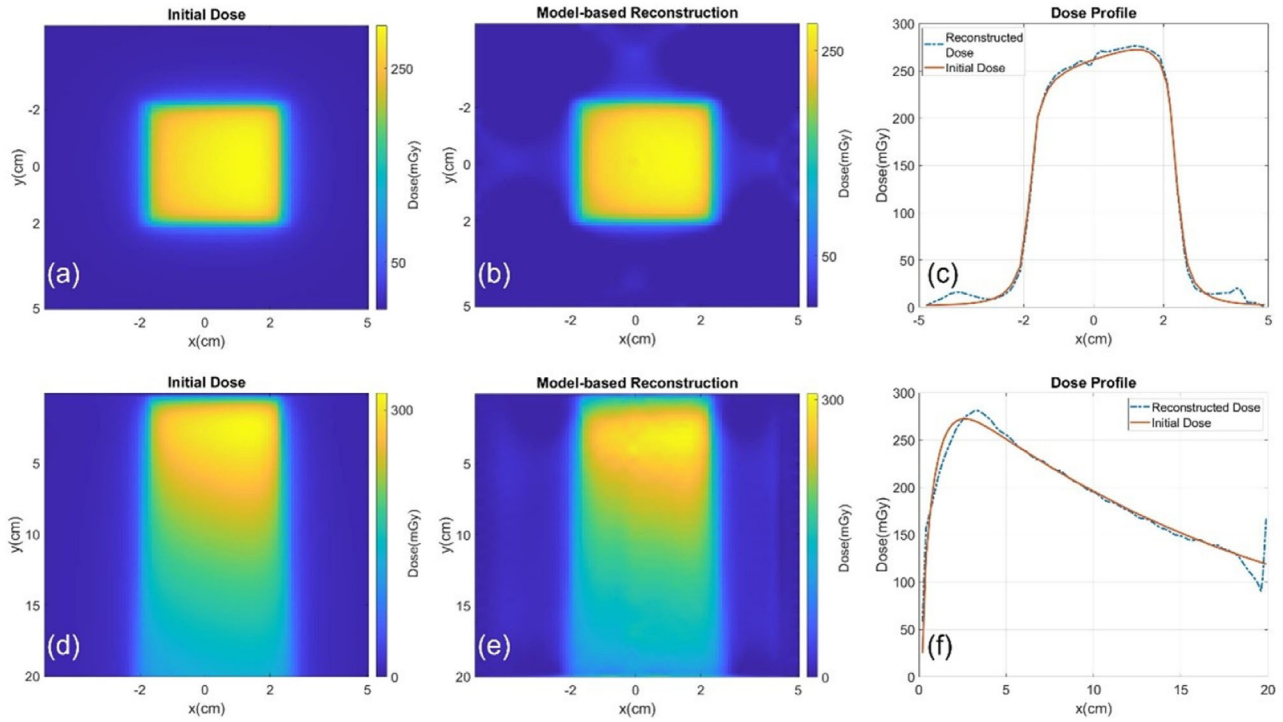

FIGURE 4 Simulated wedge reconstruction. (a) Initial dose for horizontal plane at 6 cm depth. (b) Model-based reconstruction for horizontal plane at 6 cm depth. (c) Dose profile comparison for horizontal plane at 6 cm depth. (d) Initial dose for vertical plane at isocenter. (e) Model-based reconstruction for vertical plane at isocenter. (f) Dose profile comparison for vertical plane at isocenter.

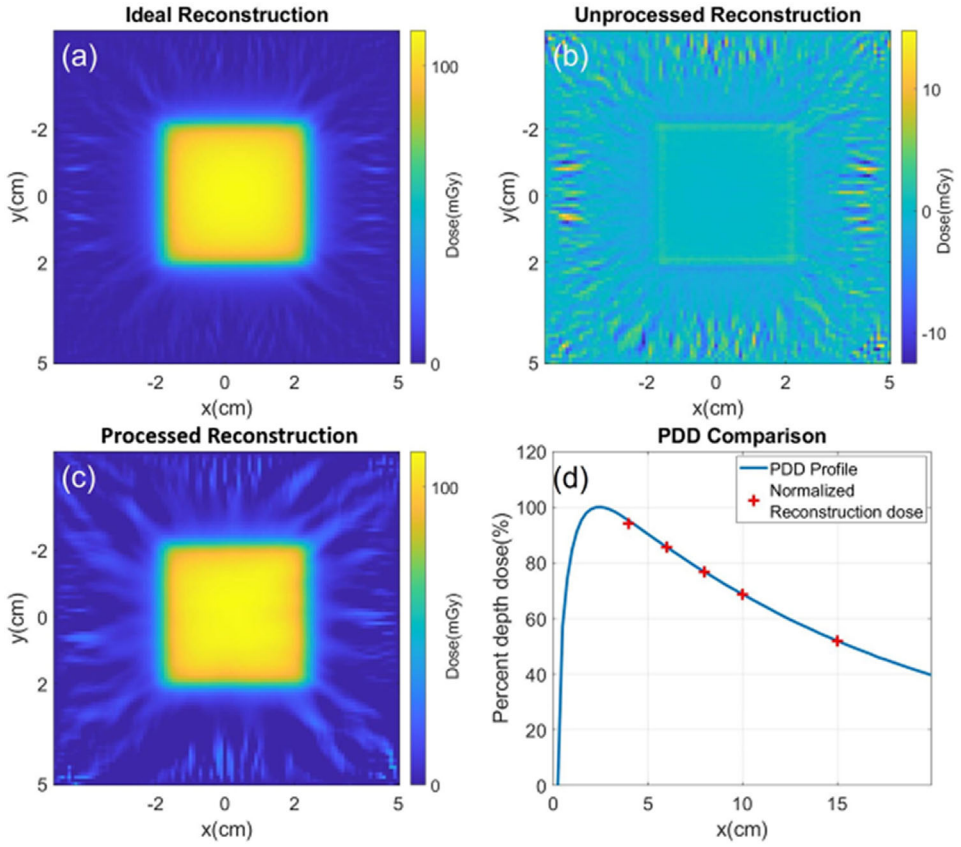

FIGURE 5 Comparison of reconstructed horizontal plane images at 6 cm depth using (a) ideal signal; (b) simulated real signal; (c) processed signal; (d) comparison of the normalized reconstruct dose and the percent depth dose (PDD) profile.

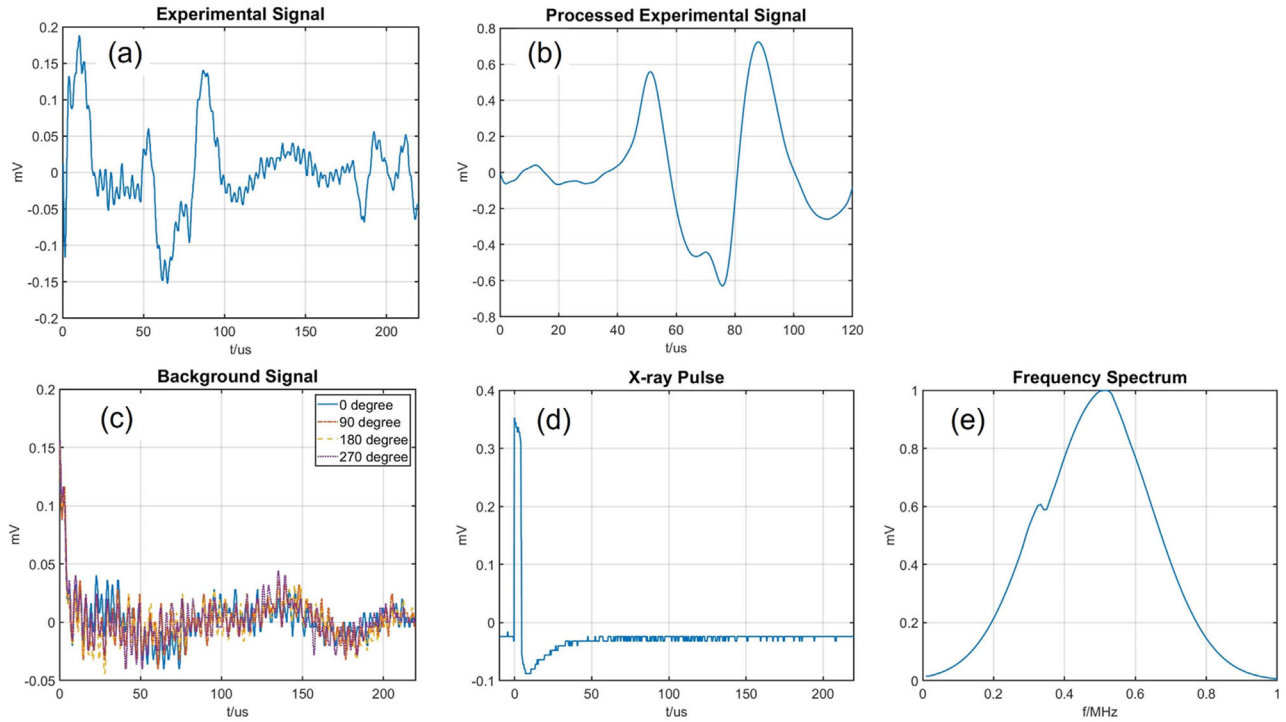

FIGURE 6 (a) Acquired experimental signal with 1–300 kHz amplifier. (b) Processed experimental signal with background noise deducted and x-ray pulse, frequency spectrum deconvoluted. (c) Background noise signal acquired at four different transducer positions: 0, 90°, 180°, 270°. (d) X-ray pulse duration signal. (e) Frequency spectrum for experiment transducer (acquired from Olympus instrumentation test).

acquired from a single transducer by rotating the LINAC head 360°. Figure 6a shows the experimental signal acquired at 6 cm depth under the water surface. The signal was acquired by averaging 512 pulses and was amplified using a 1–300 kHz amplifier. Figure 6c shows the background noises that are acquired with the LINAC collimator fully closed. The amplitude of the background noise in the figure cannot be neglected. In addition, the background signals are acquired at four different field angles. It's observed from the figure that the noises at different positions vary from each other. Therefore, each background signal is deducted from the original signal according to the time. Then, the LINAC x-ray pulse duration and transducer frequency spectrum were acquired experimentally and through documentation, respectively. The signal with background noise deducted was first denoised using 20 kHz high-pass and 200 kHz low-pass digital filter. Figure 6d shows the x-ray pulse duration file acquired by recording the head wave generated by x-ray directly hitting the Olympus transducer. This pulse signal was deconvoluted from the denoised signal. Figure 6e shows the frequency spectrum acquired from Olympus instrumentation test, which was then divided from the deconvoluted signal in the frequency domain. Figure 6b shows the processed experimental signal. After processing, the XA signal shape can be clearly observed in the processed signal plot.

Both processed and unprocessed signals shown in Figure 6 were used to reconstruct XACT image to verify the effects of our signal processing procedures. Figure 7 shows the comparison of the reconstruction results using the two signals. From the figure, it's observed that the relationship between signal unit mV and the real dose is unclear. To address this, relative pressure was used in the reconstruction results. Figure 7a is the unprocessed model-based reconstruction. Only a shadow of the radiation field can be seen in the center, which is similar to the simulation result in Figure 5b. With the processed signal, the reconstruction is much better in Figure 7b. The UBP reconstruction using the unprocessed signal shown in Figure 7c is strongly affected by the high-frequency noise. There are some improvements in the UBP reconstruction using the processed signal in Figure 7d, but artifacts still exist in the center of the radiation field. Therefore, the model-based reconstruction algorithm outperforms the UBP algorithm in this experimental study.

In order to see the quantitative dose reconstruction, three signal sets at 6, 8, and 10 cm were acquired. The reconstruction results are shown in Figure 8. Here, the PDD profile was used to calibrate the relative pressure, thus the results are shown in dose. High-quality reconstructions were obtained for the strong signals acquired at 6 and 8 cm. However, the signal at 10 cm does not have good reconstruction results due to the

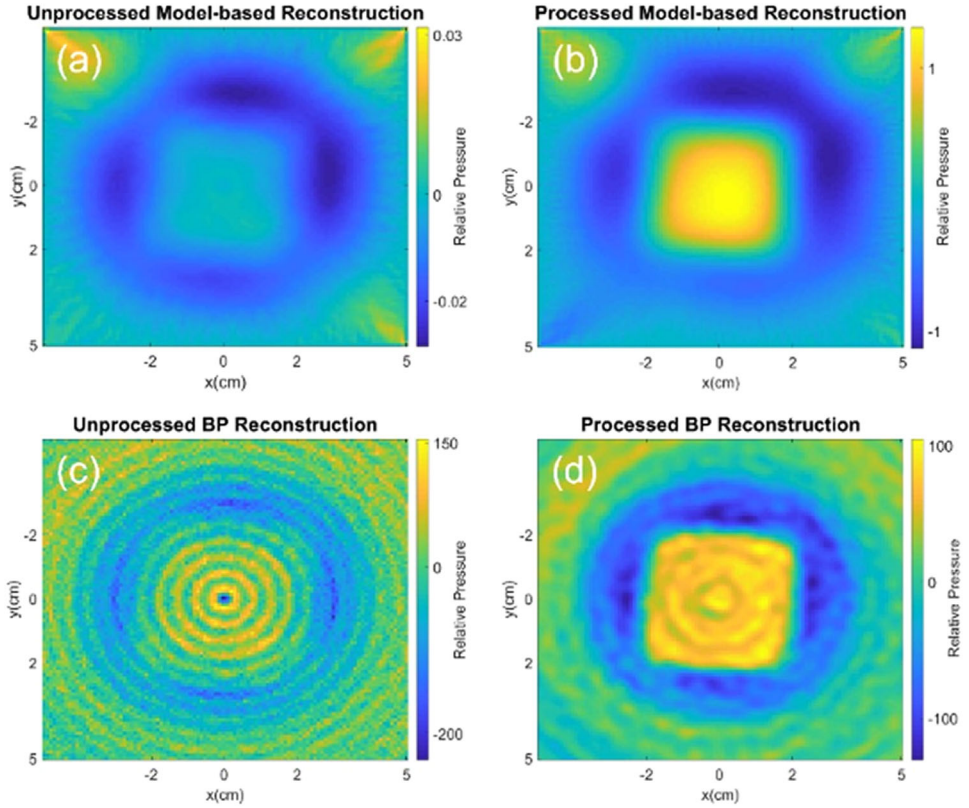

FIGURE 7 (a) Model-based reconstruction with unprocessed signal. (b) Model-based reconstruction with processed signal. (c) back-projection (BP) reconstruction with unprocessed signal. (d) BP reconstruction with processed signal.

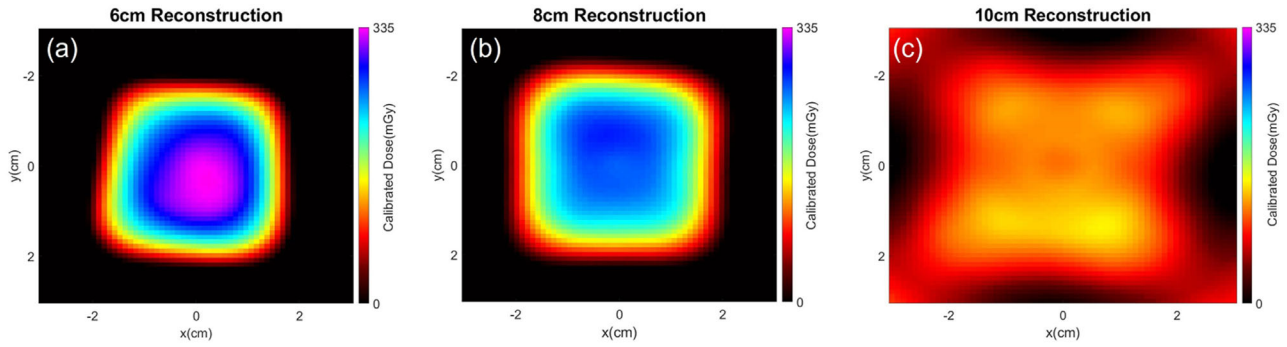

FIGURE 8 Model-based reconstruction at different depth (a) 6 cm; (b) 8 cm; (c) 10 cm. All three images are normalized using the value at PDD location in 6 cm-depth image.

signal-to-noise ratio (SNR) being too small. Nevertheless, a good radiation field shape in the 10 cm reconstruction is viewed. In addition, the reconstructed dose decreases with the increasing transducer depth, which matches the simulation results.

4 | DISCUSSION

This work first investigated the feasibility of using XACT for 3D quantitative dosimetry in vivo during RT. A discretized mathematical model was employed to simulate the generation and propagation of the XA wave in Section 2.1. For the detection of XA signal, the reception angle of the real transducer was used instead of infinite angular directivity.[20] For the reconstruction of XACT images, previous work mainly used BP algorithm.[14,19,21,49] However, BP algorithm is oversimplified as it only sums the radial projections for each transducer, which cannot quantify the dose. Therefore, model-based algorithm[31] was used to better reconstruct the quantitative dose information.

Because the acoustic wave propagated spherically, a 3D cylindrical transducer array was set up to acquire the acoustic signals from all directions. A 4 cm × 4 cm radiation field was used in the simulation as the head wave effect in 1 cm × 1 cm radiation field needed additional processing. The standard 10 cm × 10 cm radiation field was also not used as 90 transducers in a ring array will cause sparse view problems for large field size and increasing the transducer number in 3D will increase the computational cost. The model-based reconstruction results Figure 3c,f show that accurate quantitative dose can be received if the 3D signal acquisition scheme was used. It was also noted based on the reconstructions that the upper and lower parts of the reconstructed radiation field Figure 3c do not match with the initial radiation field. However, this will not be a problem as dose information is not needed at the top and bottom of the radiation field when applying XACT to the clinic. In addition, the acoustic propagation in heterogeneous medium (patient body) will be much different from homogeneous medium (water tank). The attenuation, reflection, and refraction of the acoustic waves need to be taken into account. In our previous study, simulations were completed to account for these effects.[50] For patient study feasibility, X. Wang and I. El Naqa's group demonstrated that with LINAC x-ray beam, relative dose distribution field can be reconstructed.[51] However, they pointed out that their methods mostly image the edges of the radiation field, and better algorithms are needed to get quantitative dose information.

As it is still not feasible to use large 3D cylindrical arrays in real clinic applications, a circular array simulation was done to get 2D dose images. However, the reconstructed dose was different from the initial dose distribution for the representative plane. This is because the XA signal propagates in 3D, and 2D transducer array can only get partial signals. Therefore, calibration is needed to acquire quantitative dosimetry. PDD at 6 cm depth was used to calibrate the reconstructed dose at the corresponding 2D plane. After the calibration, the quantified dose matches well with the PDD profile.

For the experimental study, we rotated the LINAC head 360° instead of rotating the transducer. This strategy can avoid water motion caused by rotating the transducer in the water tank. However, acquiring data from 90 radiation field positions can be time-consuming and the LINAC output can vary from time to time. Therefore, background signals are acquired at different experiment time points to lower the effects of the background noise. In addition, we chose to place the transducer 9 cm away from the center of the radiation field to avoid the head wave caused by the x-ray directly hitting the transducer, which can be viewed in Figure 6. Although the head wave may still affect the signal at 9 cm distance, it cannot be moved further as tests show that the SNR will decrease rapidly after 9 cm. When deciding the imaging plane, signals deeper than 4 cm were selected because the single Olympus transducer, which has an element size of 1.5 inches diameter, had to be fully immersed. Additionally, the reception angle of the transducer needs to be considered to make sure that all parts of the reception cone lie within the radiation field, which needs another 2 cm. Therefore, the highest transducer position should be 3.5 cm depth.

Different from traditional photoacoustic imaging, the LINAC x-ray pulse has a pulse duration of 4 μs, which will affect the size of the reconstructed radiation field. After deconvoluting the LINAC x-ray pulse duration and transducer frequency spectrum from the experimental signal, the reconstruction result (Figure 8) accurately localized the radiation field and displayed uniform dose distribution in the center of the radiation field. However, these results were taken by only using novel deconvolution methods provided by MATLAB. More precisive deconvolution methods, such as deep learning method,[52] can further enhance the signal and make the reconstructed radiation field more uniform. Moreover, from frequency spectrum analysis, with a 4 cm × 4 cm radiation field, the main frequency for the acquired signal lies around 100 kHz, even with a 500 kHz center frequency transducer. However, we do not currently have a transducer that has a center frequency of 100 kHz. Therefore, as was described in Section 3.3, a 1–300 kHz amplifier was used to the system to amplify the signal. Consequently, the spatial resolution of the reconstructed dose will degrade due to loss of high frequency signal. According to Jun X's[53] paper, the minimum obtainable resolution for 300 kHz is 2.5 mm, which is set to be the resolution of the reconstructed dose.

In addition, though quantitative dose reconstruction is achieved, absolute dosimetry information cannot be received directly from the reconstruction as calculations for the relationship between signal amplitude (mV) and dose (Gy) cannot be done. To get the absolute dose information, the measured signal amplitude needs to be matched to the machine output, which is calibrated using TG51[54] at a depth of 10 cm for a goal of 1 MU = 1 cGY. If the machine output per pulse is a constant value, then the total number of pulses can be counted to determine the total dose delivered at different depths using PDD curve. From the reconstructed images for different depths (Figure 8), the dose is decreasing with depth increasing. However, the reconstructed dose cannot match the PDD profile well after the calibration due to noise effect. This is because the main frequency components are mostly under 200 kHz, which is outside our transducer's bandwidth, making the signal to noise ratio not ideal. A better match between the XA signal and detector would improve the SNR. In addition, we rotated the radiation field to mimic a ring array, which took a long time and the noise pattern at different times can vary. Instead, implementing a transducer array can improve the SNR. In Zhang et al.,[51] they achieved high SNR

signals in liver with a planar transducer array that has center frequency of 0.35 MHz. Hence, we will be able to reconstruct dose more accurately in deeper fields by improving SNR.

With the rapid development of RT, more complex dose delivery plans are made, and higher dose/fraction (hypofractionation regimens) and delivery rates (FLASH-radiotherapy) are now seeing more rapid implementation. Therefore, the capability to accurately perform real-time dosimetry will only enhance the efficacy of precision radiotherapy. As the strength of the XA signal is proportional to dose and propagates spherically, XACT can potentially be used to monitor the dose delivered to certain volume during treatment. This is a particularly important feature, as dose determination for deep-seated larger volume tumors remains a challenge. Furthermore, because the XACT technique is non-invasive, it is easy to implement, and transducers can be placed around the patient during radiotherapy with no disruptions to treatment procedures. This technology dovetails well with the emerging field of ultra-high dose rate FLASH radiotherapy, where real-time dosimetry will enable improved conformality across all three (electron, photon, proton) FLASH platforms in use today. However, to apply XACT to the clinic, we need to build a complete data acquisition system to recover optimized XA signals from the system gain and background noise. Our group is currently investigating a new XACT system to get strong and noise-free signals. In addition, traceable calibration is needed for the XACT to get absolute dose. The PDD profile used in this study is an efficient tool for calibration. Furthermore, this study used a full-view data acquisition scheme to reconstruct accurate XACT images in water. However, it is often impractical to employ full-view acquisition in the clinic, and the patient anatomy structure will introduce complex heterogeneous problems to the reconstruction. New reconstruction algorithm with practical transducer arrays, such as transperineal planar arrays, are currently under investigation for clinical translation.

5 | CONCLUSIONS

The capability of using XACT for quantitative in vivo dosimetry was demonstrated through this simulation study. A model-based algorithm was applied to an XACT modality, which showed better performance than a UBP algorithm in the reconstruction of quantitative dose information. Furthermore, we demonstrated that the experimental XA signal can be used for dose reconstruction if calibrated. XA imaging has great potential to be used as a quantitative dosimetry tool in RT as well as across any modality used in current practice.

ACKNOWLEDGMENTS

Research reported in this publication was supported by the National Cancer Institute of the National Institutes of Health under Award Number (R37CA240806). The content is solely the responsibility of the authors and does not necessarily represent the official views of the National Institutes of Health. Approximately, $500k of federal funds supported the effort (50%) on this project. Approximately, $200k of American Cancer Society (133697-RSG-19-110-01-CCE) funds supported a portion of the effort (45%) on this project. The authors would like to acknowledge the support from UCI Chao Family Comprehensive Cancer Center (P30CA062203) (5%).

CONFLICT OF INTEREST STATEMENT

The authors declare no conflicts of interest.

REFERENCES

1. Khan FM, Gibbons JP. *Khan's the Physics of Radiation Therapy*. Lippincott Williams & Wilkins; 2014.
2. Prince JL, Links J. *Medical Imaging Signals and Systems*. Prentice Hall; 2006.
3. Mohan R, Barest G, Brewster LJ, et al. A comprehensive three-dimensional radiation treatment planning system. *Int J Radiat Oncol Biol Phys*. 1988;15(2):481-495. doi:10.1016/S0360-3016(98)90033-5
4. Height R, Khoo V, Lawford C, et al. The dosimetric consequences of anatomic changes in head and neck radiotherapy patients. *J Med Imaging Radiat Oncol*. 2010;54(5):497-504. doi:10.1111/j.1754-9485.2010.02209.x
5. Shimohigashi Y, Toya R, Saito T, et al. Tumor motion changes in stereotactic body radiotherapy for liver tumors: an evaluation based on four-dimensional cone-beam computed tomography and fiducial markers. *Radiat Oncol*. 2017;12(1):61. doi:10.1186/s13014-017-0799-7
6. Hughes JR, Parsons JL. FLASH Radiotherapy: current knowledge and future insights using proton-beam therapy. *Int J Mol Sci*. 2020;21(18):E6492. doi:10.3390/ijms21186492
7. Paquin D, Levy D, Xing L. Multiscale registration of planning CT and daily cone beam CT images for adaptive radiation therapy. *Med Phys*. 2009;36(1):4-11. doi:10.1118/1.3026602
8. Mijnheer B. State of the art of in vivo dosimetry. *Radiat Prot Dosim*. 2008;131(1):117-122. doi:10.1093/rpd/ncn231
9. Yan D, Vicini F, Wong J, Martinez A. Adaptive radiation therapy. *Phys Med Biol*. 1997;42(1):123-132. doi:10.1088/0031-9155/42/1/008
10. In vivo dosimetry in external beam radiotherapy – PubMed. Accessed November 17, 2021. https://pubmed.ncbi.nlm.nih.gov/23822404/
11. Nailon WH, Welsh D, McDonald K, et al. EPID-based in vivo dosimetry using Dosimetry Check™: overview and clinical experience in a 5-yr study including breast, lung, prostate, and head and neck cancer patients. *J Appl Clin Med Phys*. 2019;20(1):6-16. doi:10.1002/acm2.12441
12. Feng B, Yu L, Mo E, et al. Evaluation of daily CT for EPID-based transit in vivo dosimetry. *Front Oncol*. 2021;11. Accessed January 12, 2023. doi:https://www.frontiersin.org/articles/10.3389/fonc.2021.782263
13. Rivera T. Thermoluminescence in medical dosimetry. *Appl Radiat Isot*. 2012;71:30-34. doi:10.1016/j.apradiso.2012.04.018
14. Xiang L, Han B, Carpenter C, Pratx G, Kuang Y, Xing L. x-ray acoustic computed tomography with pulsed x-ray beam from a

medical linear accelerator. *Med Phys*. 2013;40(1):010701. doi:10.1118/1.4771935
15. Rosencwaig A, Gersho A. Theory of the photoacoustic effect with solids. *J Appl Phys*. 1976;47(1):64-69. doi:10.1063/1.322296
16. Xu M, Wang LV. Photoacoustic imaging in biomedicine. *Rev Sci Instrum*. 2006;77(4):041101. doi:10.1063/1.2195024
17. Hickling S, Xiang L, Jones KC, et al. Ionizing radiation-induced acoustics for radiotherapy and diagnostic radiology applications. *Med Phys*. 2018;45(7):e707-e721. doi:10.1002/mp.12929
18. Hickling S, Léger P, El Naqa I. On the detectability of acoustic waves induced following irradiation by a radiotherapy linear accelerator. *IEEE Trans Ultrason Ferroelectr Freq Control*. 2016;63(5):683-690. doi:10.1109/TUFFC.2016.2528960
19. Wang M, Samant P, Wang S, et al. Toward in vivo dosimetry for prostate radiotherapy with a transperineal ultrasound array: a simulation study. *IEEE Trans Radiat Plasma Med Sci*. 2021;5(3):373-382. doi:10.1109/TRPMS.2020.3015109
20. Forghani F, Mahl A, Patton TJ, et al. Simulation of x-ray-induced acoustic imaging for absolute dosimetry: accuracy of image reconstruction methods. *Med Phys*. 2020;47(3):1280-1290. doi:10.1002/mp.13961
21. Experimental evaluation of x-ray acoustic computed tomography for radiotherapy dosimetry applications – Hickling – 2017 – Medical Physics – Wiley Online Library. Accessed September 2, 2021. https://aapm.onlinelibrary.wiley.com/doi/full/10.1002/mp.12039
22. Lei H, Zhang W, Oraiqat I, et al. Toward in vivo dosimetry in external beam radiotherapy using x-ray acoustic computed tomography: a soft-tissue phantom study validation. *Med Phys*. 2018;45(9):4191-4200. doi:10.1002/mp.13070
23. Davidian M. Dose calibration. In: *Encyclopedia of Environmetrics*. John Wiley & Sons, Ltd; 2006. doi:10.1002/9780470057339.vad038
24. Sarvazyan AP, Urban MW, Greenleaf JF. Acoustic waves in medical imaging and diagnostics. *Ultrasound Med Biol*. 2013;39(7):1133-1146. doi:10.1016/j.ultrasmedbio.2013.02.006
25. Irisawa K, Hirasawa T, Hirota K, Tsujita K, Ishihara M. Influence of laser pulse width to the photoacoustic temporal waveform and the image resolution with a solid-state excitation laser. *Photons Plus Ultrasound: Imaging and Sensing 2012*. SPIE; 2012;8223:544-551. doi:10.1117/12.907714
26. Agano T, Kuniyil Ajith Singh M, Nagaoka R, Awazu K. Effect of light pulse width on frequency characteristics of photoacoustic signal-an experimental study using a pulse-width tunable LED-based photoacoustic imaging system. *Int J Eng Technol*. 2018;7:4300-4303. doi:10.14419/ijet.v7i4.19907
27. Intro. to Signal Processing: Deconvolution. Accessed November 17, 2021. https://www.grace.umd.edu/~toh/spectrum/Deconvolution.html
28. 3D X-ray-induced acoustic computed tomography (3D XACT) – University of California Irvine. Accessed November 18, 2021. https://uci.primo.exlibrisgroup.com
29. Ku G, Wang X, Stoica G, Wang LV. Multiple-bandwidth photoacoustic tomography. *Phys Med Biol*. 2004;49(7):1329-1338. doi:10.1088/0031-9155/49/7/018
30. Buehler A, Deán-Ben XL, Razansky D, Ntziachristos V. Volumetric optoacoustic imaging with multi-bandwidth deconvolution. *IEEE Trans Med Imaging*. 2014;33(4):814-821. doi:10.1109/TMI.2013.2282173
31. Dean-Ben XL, Ntziachristos V, Razansky D. Acceleration of optoacoustic model-based reconstruction using angular image discretization. *IEEE Trans Med Imaging*. 2012;31(5):1154-1162. doi:10.1109/TMI.2012.2187460
32. Xu M, Wang LV. Universal back-projection algorithm for photoacoustic computed tomography. *Phys Rev E Stat Nonlin Soft Matter Phys*. 2005;71(1 Pt 2):016706. doi:10.1103/PhysRevE.71.016706
33. Zhang Y, Wang Y. An improved filtered back-projection algorithm for photoacoustic tomography. 2011 5th International Conference on Bioinformatics and Biomedical Engineering, 2011:1-4. doi:10.1109/icbbe.2011.5780223
34. Deán-Ben XL, Buehler A, Ntziachristos V, Razansky D. Accurate model-based reconstruction algorithm for three-dimensional optoacoustic tomography. *IEEE Trans Med Imaging*. 2012;31(10):1922-1928. doi:10.1109/TMI.2012.2208471
35. Ding L, Razansky D, Dean-Ben XL. Model-based reconstruction of large three-dimensional optoacoustic datasets. *IEEE Trans Med Imaging*. 2020;39(9):2931-2940. doi:10.1109/TMI.2020.2981835
36. Lutzweiler C, Deán-Ben XL, Razansky D. Expediting model-based optoacoustic reconstructions with tomographic symmetries. *Med Phys*. 2014;41(1):013302. doi:10.1118/1.4846055
37. Treeby BE, Cox BT. k-Wave: MATLAB toolbox for the simulation and reconstruction of photoacoustic wave fields. *J Biomed Opt*. 2010;15(2):021314. doi:10.1117/1.3360308
38. Thomas J, Amir R, Englmeier K-H, Alexander D, Miguel AAC, Daniel R, Vasilis N. Interpolated model-matrix optoacoustic tomography of the mouse brain. *Appl Phys Lett*. 98(16). Accessed January 12, 2023. https://aip.scitation.org/doi/10.1063/1.3579156
39. Clason C, Kaltenbacher B, Resmerita E. Regularization of Ill-Posed Problems with Non-negative Solutions. In: Bauschke HH, Burachik RS, Luke DR, eds. *Splitting Algorithms, Modern Operator Theory, and Applications*. Springer International Publishing; 2019:113-135. doi:10.1007/978-3-030-25939-6_5
40. Pandey PK, Wang S, Aggrawal HO, Bjegovic K, Boucher S, Xiang L. Model-based x-ray induced acoustic computed tomography. *IEEE Trans Ultrason Ferroelectr Freq Control*. 2021;68(12):3560-3569. doi:10.1109/TUFFC.2021.3098501
41. The MathWorks, Inc. Solve system of linear equations – least-squares method – MATLAB lsqr. 2022. Accessed February 1, 2023. https://www.mathworks.com/help/matlab/ref/lsqr.html
42. Krishna GS, Srinivas V, Ayyangar KM, Reddy PY. Comparative study of old and new versions of treatment planning system using dose volume histogram indices of clinical plans. *J Med Phys*. 2016;41(3):192-197. doi:10.4103/0971-6203.189489
43. Rosnitskiy P, Yuldashev P, Khokhlova V. Effect of the angular aperture of medical ultrasound transducers on the parameters of nonlinear ultrasound field with shocks at the focus. *Acoust Phys*. 2015;61:301-307. doi:10.1134/S1063771015030148
44. Yumpu.com. Ultrasonic Transducers Technical Notes – Olympus. yumpu.com. Accessed September 2, 2021. https://www.yumpu.com/en/document/view/10788380/ultrasonic-transducers-technical-notes-olympus
45. Sun L, Jiang Z, Chang Y, Ren L. Building a patient-specific model using transfer learning for four-dimensional cone beam computed tomography augmentation. *Quant Imaging Med Surg*. 2021;11(2):540.
46. The MathWorks, Inc. Dependence of photoacoustic speckles on boundary roughness. 2022. Accessed January 27, 2023. https://www.spiedigitallibrary.org/journals/journal-of-biomedical-optics/volume-17/issue-4/046009/Dependence-of-photoacoustic-speckles-on-boundary-roughness/10.1117/1.JBO.17.4.046009.full?SSO=1
47. The MathWorks, Inc. Root-mean-square error between arrays – MATLAB rmse. 2022. Accessed March 23, 2023. https://www.mathworks.com/help/matlab/ref/rmse.html
48. The MathWorks, Inc. Structural similarity (SSIM) index for measuring image quality – MATLAB ssim. 2022. Accessed March 23, 2023. https://www.mathworks.com/help/images/ref/ssim.html
49. The MathWorks, Inc. High resolution x-ray-induced acoustic tomography | Scientific reports. 2022. Accessed September 8, 2021. https://www.nature.com/articles/srep26118
50. Jiang Z, Sun L, Yao W, Wu QJ, Xiang L, Ren L. 3D in vivo dose verification in prostate proton therapy with deep learning-based proton-acoustic imaging. *Phys Med Biol*. 2022;67(21):215012. doi:10.1088/1361-6560/ac9881

51. Zhang W, Oraiqat I, Litzenberg D, et al. Real-time, volumetric imaging of radiation dose delivery deep into the liver during cancer treatment. *Nat Biotechnol*. 2023:1-8. Published online January 2. doi:10.1038/s41587-022-01593-8
52. Gutta S, Kadimesetty VS, Kalva SK, Pramanik M, Ganapathy S, Yalavarthy PK. Deep neural network-based bandwidth enhancement of photoacoustic data. *J Biomed Opt*. 2017;22(11):1-7. doi:10.1117/1.JBO.22.11.116001
53. Xia J, Yao J, Wang LV. Photoacoustic tomography: principles and advances. *Electromagn Waves (Camb)*. 2014;147:1-22.
54. Almond PR, Biggs PJ, Coursey BM, et al. AAPM's TG-51 protocol for clinical reference dosimetry of high-energy photon and electron beams. *Med Phys*. 1999;26(9):1847-1870. doi:10.1118/1.598691

How to cite this article: Sun L, Gonzalez G, Pandey PK, et al. Towards quantitative in vivo dosimetry using x-ray acoustic computed tomography. *Med Phys*. 2023;50:6894–6907. https://doi.org/10.1002/mp.16476